UNIABUJA Journal of Engineering and Technology
https://ujet.uniabuja.edu.ng/
ISSN: 2714-3236 (Online); 2714-3228 (Print)
Volume 2, Issue 2, 2025; 83-98

Investigating the Microstructural Variation Between the Uncoated and Coated Ti27at. %Nb and Ti-25at. %Ta Alloys at the Selected Parameters

Ishiaka S. ARUDI[1*] and Samson BALOGUN[2]

[1]Department of Mechanical Engineering, Faculty of Engineering, University of Abuja, Abuja, Nigeria
[2]Department of Civil Engineering, Faculty of Engineering, University of Abuja, Abuja, Nigeria

[1]shuaibu.ishiaka@uniabuja.edu.ng, [2]samson.balogun@uniabuja.edu.ng

Abstract
In this study, microstructural investigations and characterization of coated and uncoated Titanium Niobium (Ti-27at. %Nb) and Titanium Tantalum (Ti-25at. %Ta) alloys samples were conducted to assess the coated and uncoated alloys. The samples were cut into the required sizes, grounded and polished for materials characterization testing and coating process. The choice material for coating the samples was Titanium nitride (TiN). The coating process was designed by applying Taguchi method to find the appropriate number of experiments using Magnetron sputtering. Microstructural characterisation was done after the coating was applied using the Taguchi orthogonal array (OA) method and Physical Vapour Deposition (PVD) technology. Using Electron Backscatter Diffraction (EBSD) to characterise the as-received alloys, it was discovered that characteristic microstructural and textural gradients had formed, with grain sizes of 134 µm, 38 µm, and 72 µm for Ti-27at% Nb and Ti-25at%Ta, respectively. The microstructural investigations of the optimized Ti-27at. %Nb and Ti-25at. %Ta coated with Ti/TiN performed employing XRD, FESEM, EDX and AFM techniques revealed the morphological, elemental composition, phases and roughness of the alloys. The influence of the recommended parameter combinations on crystallite structure was established and the average crystallites (grain) size of the improved samples as presented by the XRD analysis were determined. The various thicknesses of coated Ti-27at. %Nb and Ti-25at. %Ta samples that give optimal adhesion strength are 1.92µm, 1.78 µm and for optimal surface hardness are 1.73 µm, 1.91 µm respectively. Results of AFM analysis showed that the coated Ti-27at. %Nb to obtain optimal adhesion has lower surface roughness (Ra) of 27.04 nm, than the coating to obtain optimal hardness which is 44.07 nm while the coated Ti-25at. %Ta to obtain optimal hardness has lower surface roughness of 32.20 nm than the coating for optimal adhesion with roughness of 33.56 nm.

Keywords: *Microstructural, coating thickness, surface hardness, adhesion strength.*

1.0 Introduction

A number of bones with specific functions in physical structure make up the skeletal system, which is the interior architecture of the human body. The bone deteriorates due to social interactions, physiological processes, trauma, and illness. Arthritis is a serious condition that primarily affects the elderly and occasionally younger people. It can result in acute discomfort and inability to move as well as negatively impact the standard of living for those who are affected (Manivasagam et al., 2010). In addition to those who are afflicted with the illness, young, nimble individuals like athletes frequently require bioimplant replacements because of fractures and severe strain. The intricate issues with bioimplants have been related to their interactions with bone and tissue and also their interface with biological surroundings of diverse physico-chemical nature (Manivasagam et al., 2010). The preferred biomaterial must interact properly with tissue cells and be absorbed by the body without triggering immunological rejection. A substance that has been modified for use in medicine is called a biomaterial (Tugulu et al. 2010).

Biomaterials are intended to possess low elastic modulus, super elasticity, shape memory effect, and wear resistance in the context of biomedical technology and tissue engineering. The use of nickel in biomedical implants must also be avoided, as well as any negative impacts that can cause corrosion, wear, leaching, or other problems. (Hermawan et al., 2011). Therefore, developing Ni-free, safe alloys for use in biomedical applications is very crucial

Many additional non-toxic and β-stabilizing elements, including Mo, Nb, Pt, Sn, Ta and Zr, which may prove ideal for biomedical applications, have been the subject of extensive research on Titanium alloys (Wang et al. 2010). Nb and Ta are preferred over pure Ti as alloying elements for biomaterial implants because of their better electrochemical properties and biocompatibility. Furthermore, Ta exhibits minimal ion release and outstanding corrosion resistance (Chien et al., 2016). According to earlier research (Xu et al., 2013). Ti-Nb has the lowest elastic modulus, most promising shape memory effect, highest compatibility of any alloy being researched for biomedical purposes. Ti-Ta alloy is an excellent alternative to Ti-Nb for prospective use for

Received: 03-02-2025 / Accepted: 10-03-2025 / Published: 24-05-2025
https://doi.org/10.70118/ujet.2025.0202.09

medical purposes in the future. In addition to its outstanding biocompatibility and non-toxicity, Ti-Ta possesses an elastic modulus that is similar to that of Ti-Nb, which is crucial for implant materials. According to Brunette et al. (2012), out of all the biocompatibility metrics that were investigated, the Ti-Ta had the best biocompatibility. Coating the surface of these alloys with a biocompatible material can improve their properties.

This study uses X-ray diffraction (XRD), electron backscatter diffraction (EBSD), and field emission scanning electron microscopy (FESEM) equipped with energy-dispersive X-ray spectroscopy (EDS) to investigate the microstructure variation of the uncoated and coated Ti-27at. %Nb and Ti-25at. %Ta samples at the selected parameters. The goal is to coat TiN on Ti-27 at %Nb, and Ti-25 at % Ta by magnetron sputtering physical vapour deposition (MSPVD), and to use EBSD, FESEM/EDS, XRD, and AFM to examine the uncoated and coated Ti-27 at %Nb, and Ti-25 at % Ta alloys.

2.0 Materials and Methods

Optical microscopy, Field Emission-Scanning Electron Microscopy (FESEM) equipped with energy-dispersive X-ray spectroscopy (EDS), and X-ray diffraction (XRD) were used to characterize the materials of coated and uncoated samples. The adhesion tests were conducted with the micro scratch test machine to ascertain the adhesion strength of the coated samples, while the mechanical testing, such as the hardness of the alloys, were assessed by the micro hardness test machine.

2.1 Materials

In this investigation, Ti-27at.%Nb and Ti-25at.%Ta samples were utilized as substrates. The compositions of the materials were selected based on the phase diagram and work done by other researchers (de Souza and Robin, 2003; Massalski, *et al.*, 1990; Štěpán and Losertová, 2011), indicating that the alloys have corrosion resistance, biocompatibility and hardness as the required properties, and may be used for biomedical purposes. Ti-27at. %Nb and Ti-25at. %Ta was supplied by Edgetech Industries LLC, Fl. USA, while Ti-51at. %Ni was supplied by Stanford Advanced Materials, USA. All the alloys were produced by hot-pressing method and supplied in sheet plate form with a dimension of 3mm thickness, 125mm width and 125mm length. The Ti used as a target for the PVD coating was of 99.995% purity with 101.6mm diameter and 3.18mm thickness.

2.2 Methods

2.2.1 Cutting

The as-received materials were cut into 15 mm x 15 mm using electric discharge machine, to obtain specimens for a mechanical test, coating process, and materials characterization using XRD and FESEM/EDS techniques. The cut samples for materials characterization were hot mounted in an automatic mounting press for easy handling to further prepare them for grinding and polishing.

2.2.2 Grinding, Polishing and Etching

The purpose of grinding is to remove the surface solid impurities and correct the surface irregularities to obtain a flat and relatively smooth surface, which are prerequisite for the microscopic examination of the material at different magnifications. The mounted samples which were 15 mm × 15 mm × 3 mm in size were ground using grinding/polishing machine equipped with silicon carbide (Electrochemistry, *et al.*, 2010) abrasive papers with grit numbers from 220, 500, 1000, 1500.

2.3 Design of experiment

Ti-27at. %Nb, and Ti-25at. %Ta may be effectively coated utilizing a variety of deposition settings in the physical vapor deposition (PVD) technique of coating. To obtain the intended findings using Ta substrates, a strong experimental design preparation is required. The most crucial phase of an experiment's design is the choice of control elements. In order to detect non-significant variables early on, a number of potential factors were included. In this case, nitrogen flow rate, substrate temperature, DC power, and bias voltage were chosen as the deposition parameters to function as control variables. Taguchi builds a standard orthogonal array (OA) in order to satisfy this need.

2.4 Materials Characterization

Materials characterization and microstructural analysis were performed using standard equipment, namely optical microscope, SEM, EDS, and XRD.

2.4.1 Electro Back-Scattered Diffraction (EBSD)

Grain size, crystal orientation, grain boundary orientation angles, and texture evolution were measured using an Electro Back-Scattered Diffraction (EBSD) system.

Received: 03-02-2025 / Accepted: 10-03-2025 / Published: 24-05-2025

https://doi.org/10.70118/ujet.2025.0202.09

2.4.2 Field Emission Scanning Electron Microscopy (FESEM)

A Zeiss Auriga FESEM was used to analyse the surface morphology, cross-sectional structures, and images of the uncoated and coated samples to determine the thickness of the coating layer.

2.4.3 Energy Dispersive X-Ray spectroscopy (EDS)

The elemental compositions of coated and uncoated samples were determined using EDS.

2.4.4 X-Ray Diffractometry (XRD)

XRD analyses were performed to ascertain the phases and crystal structure of the samples and the Ti/TiN coating. With a step of 0.10°, the scanning angle 2θ ranged from 30° to 90°, while the grazing angle was 1O. Peaks were used to depict the diffraction pattern that was produced. The Rigaku 2015 PDXL computer program includes the International Centre for Diffraction Data (ICDD) database, which was used to identify the XRD peak phases.

2.5 Microhardness test

The surface hardness of the uncoated and TiN-coated alloys was measured using a microhardness tester (SHIMADZU Micro Hardness Tester, HMV-2 Series). The specimen under examination was set up atop an anvil featuring a screw thread base. In order to conduct the test, a square-based diamond pyramid indenter with opposing sides that converged at an angle of 136^0 at the apex was subjected to a regulated force of 1.961N(HV0.2) for five seconds. Under a microscope, the resulting indentation diagonal was measured. Three times around the specimens, the aforementioned procedures were carried out, and the average Vickers hardness value was noted.

3.0 Results and Discussions

This section is about the results of the experiments conducted during this research. The results and the effects of MSPVD parameters on the properties of the samples coated with Ti /TiN, their surface morphology, hardness, adhesion strength and thickness of the coating are discussed.

3.1 Characterization of Ti-27at. %Nb and Ti-25at. %Ta samples

The microstructures and phase constitution of the samples were investigated by examining the materials using EBSD, SEM/EDS and XRD equipment. The investigation was necessitated by the need to verify the as-received alloys status before they could be utilised in coating process.

3.2 Microstructural assessment of Ti-27at. %Nb alloy both uncoated and Ti/TiN coated

3.2.1 Analysis of uncoated Ti-27at. %Nb alloy

Figure 1(a) displays the microstructure and microtexture of the as-received Ti-27 at% Nb as measured by EBSD. Equiaxed β grains and a random texture are seen in the mapping. The α phase forms as fine and dominating coarse acicular facets inside the equiaxial β grains. A mis-orientation angle greater than 4^o was used to define the grain boundary (Figure 1(a)). With a greater number fraction of 0.811, the phase fraction mapping displayed in Figure 1(b) indicates that the β phase is dominating. The data provided by EBSD indicate that the grain size distribution is depicted in Figure 2, with an average grain size of 38μm.

Received: 03-02-2025 / Accepted: 10-03-2025 / Published: 24-05-2025

https://doi.org/10.70118/ujet.2025.0202.09

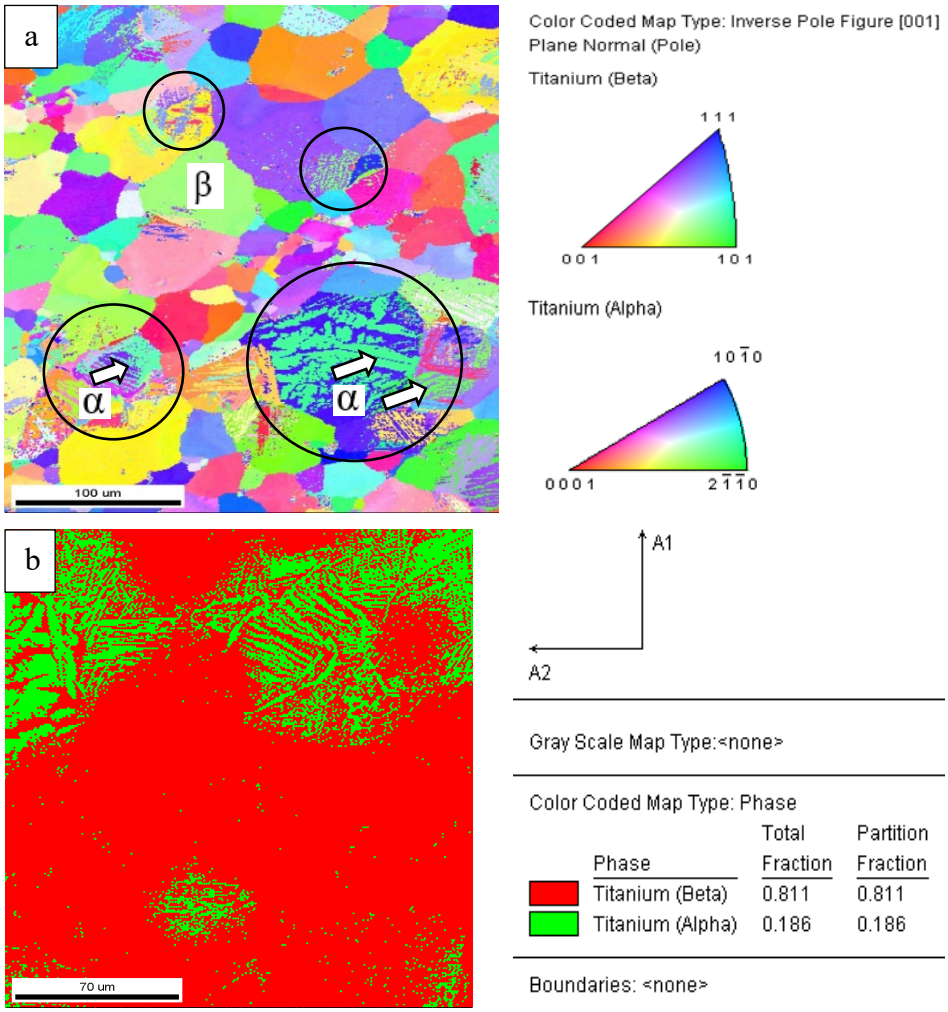

Figure 1. The Ti-27 at %Nb alloy's EBSD inverse pole figure orientation maps (a) reveal the equiaxed β grains and random texture, while the phase fraction mapping (b) shows the same pattern.

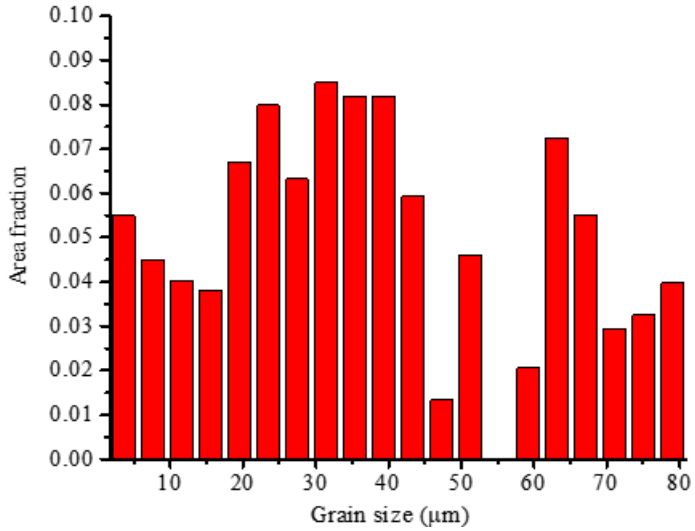

Figure 2. Grain size distribution of Ti-27at. %Nb

Figure 3 is the FESEM micrograph of Ti-27at. %Nb. The EDS analysis results revealed that the grey area, such as point **5**, is the residue of undissolved Nb powder, which is confirmed by spectrum 5 with 96.71at% niobium in the EDS point analysis shown in Figure 4. The black spots encapsulated by white regions in points **2** and **6** are oxides with 76.23 at% Oxygen and 90.73 at% Oxygen respectively, which are likely to be formed during the sintering process. The dark matrix marked point **4** is β TiNb phase with 78.80at%Ti and 22.01at%Nb as revealed in spectrum **4**, which shows that Nb wholly dissolved into the matrix in that region. The dark region marked point **1** in the acicular grain shape structure revealed α phase, having 96.37at %Ti composition. At point **3**, the lath grain shape showed a secondary α phase with 84.71at% Ti and 14.47at%Nb

Received: 03-02-2025 / Accepted: 10-03-2025 / Published: 24-05-2025

https://doi.org/10.70118/ujet.2025.0202.09

as shown in spectrum **3**. The undissolved Nb element found in the Ti-27at% Nb microstructure suggests that the alloy's production process involved incomplete diffusion.

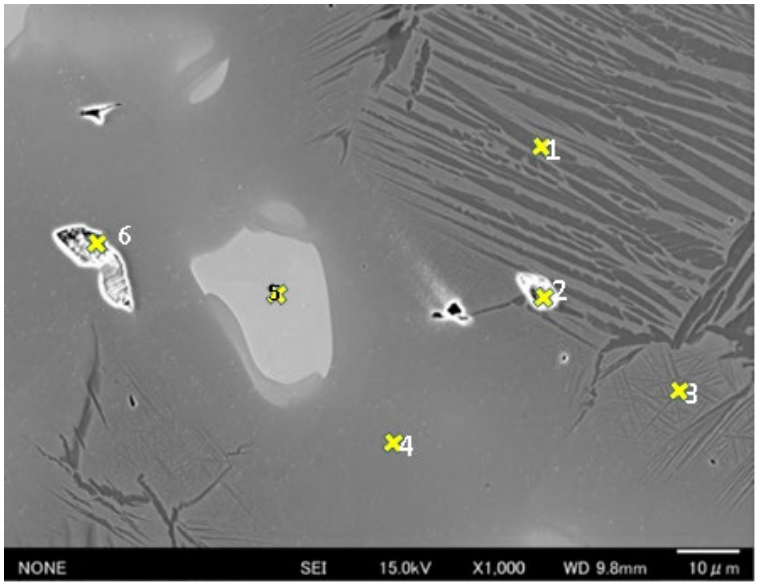

Figure 3. FESEM of elemental distribution of Ti-27at %Nb alloy

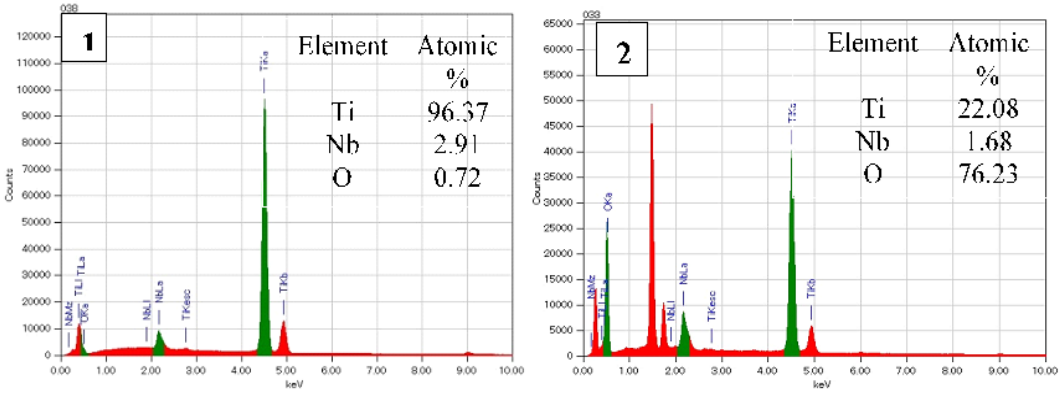

Received: 03-02-2025 / Accepted: 10-03-2025 / Published: 24-05-2025
https://doi.org/10.70118/ujet.2025.0202.09

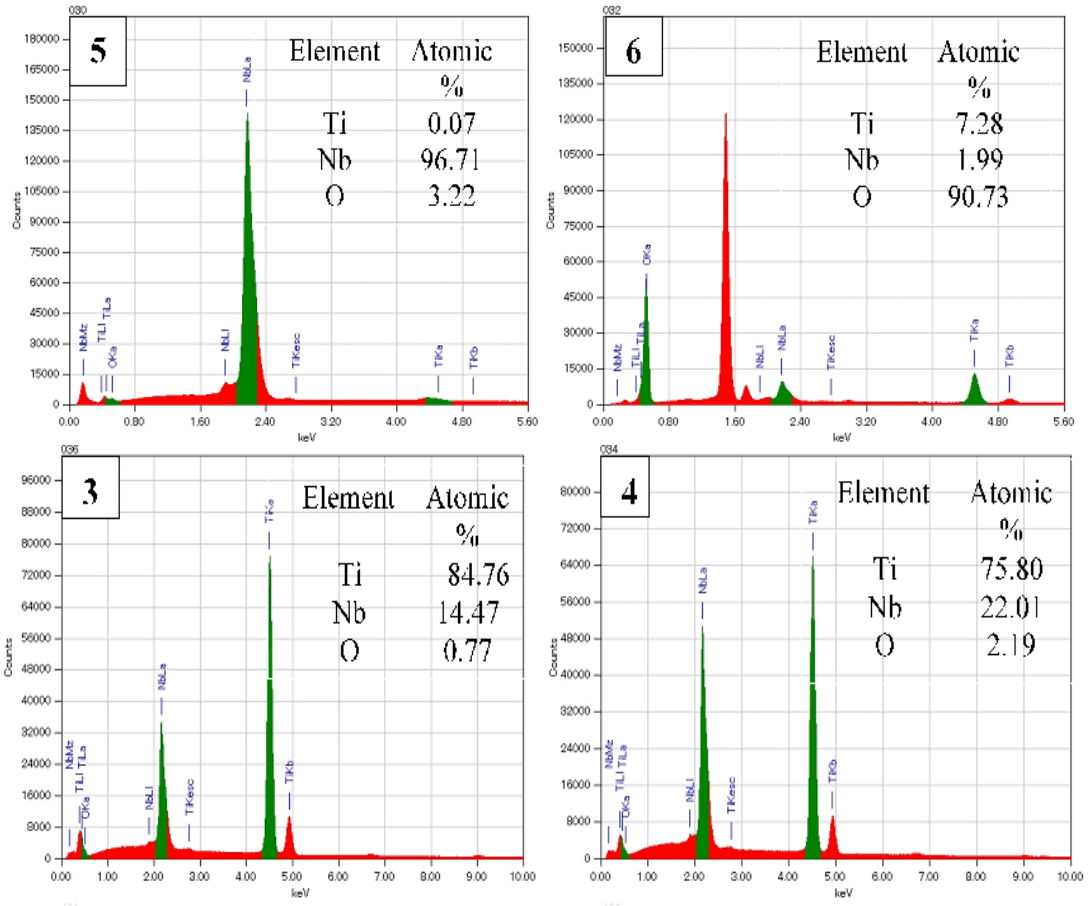

Figure 4. EDS of the elemental distribution of Ti-27%Nb alloy

The phase identification of Ti-27at. %Nb sample was investigated using XRD analysis. The XRD results shown in Figure 5 reveal that the alloy is predominantly β phase, with peak β (110) being the most prominent of all peaks. The presence of only β phase shows that the alloy was solution-treated for a significant period and subjected to aging treatment at high temperature (Lopes *et al.*, 2011; Wang *et al.*, 2014a).

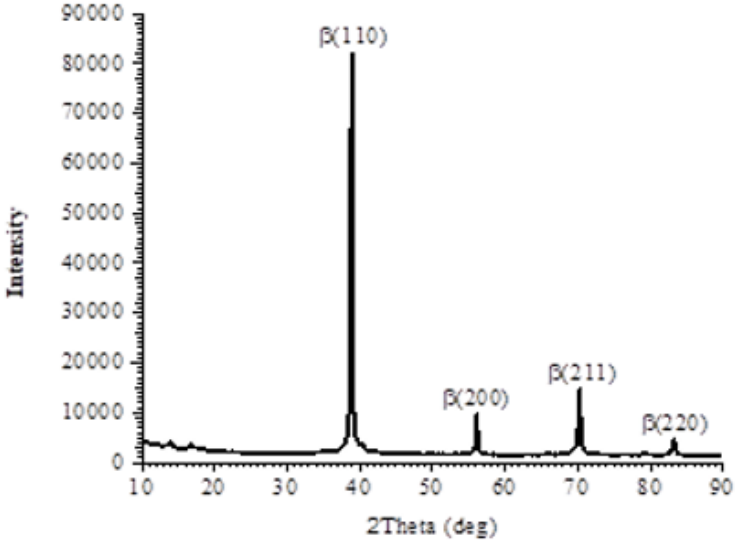

Figure 5. XRD spectrum of Ti-27at. %Nb alloy

3.2.2 Analysis of Ti-27at. %Nb Alloy Coated with Ti/TiN Using XRD

The XRD patterns of Ti/TiN coatings on Ti-27 at %Nb alloy are displayed in Figure 6. The ideal combination parameters employed to maximize adhesion strength and surface hardness were 300W, 150oC, 75V, 6.7sccm, and 370W, 150oC, 75V, and 4.7sccm, respectively. The face-centred cubic (FCC) crystal planes with only TiN peaks present are indicated by the four primary orientations, such as (111), (200), (220), and (311), which are found at 2θ of 36.61O, 42.53O, 61.90O, and 74.00O (de Sousa *et al.*, 2015).

Received: 03-02-2025 / Accepted: 10-03-2025 / Published: 24-05-2025

https://doi.org/10.70118/ujet.2025.0202.09

Figure 6(b) shows the presence of Ti (110) and Ti (211) peaks in the adhesion coating, indicating the Ti bond coat's preferred orientation. It is known that there is always competition between various energies, such as the strain energy (111), lowest surface energy (200), and the stopping energy (220) of different lattice planes. It is expected that the film grows in the direction with the lowest sum of surface energy (200) and strain energy (111). The peak intensities of (111), (200), and (220) planes shown in Figure 6(a) and (b) are at variance, which could be attributed to the difference in DC power and nitrogen flow rate. At 370W and 4.7sccm, the TiN exhibits a strong (200) orientation and a relatively weak (111) and (220) orientations, while at 300W and 6.7sccm, strong (111), relatively strong (220) and weak (200) orientations were observed.

Escalona *et al.* (2021) state that for lesser TiN thicknesses of 1.73µm, the TiN (200) orientation with the lowest surface energy is chosen, and that the surface energy term is substantial. As the film thickness grows to 1.92µm, the strain energy difference between various lattice planes becomes dominant and the preferred orientation becomes evident (111); these results are similar to the results of thickness for adhesion strength and surface hardness that were seen in the TiN coatings. However, at 300W and 6.7 with (111) preferred orientation and 370W and 4.7sccm with (200) preferred orientation, the coating thickness was 1.92µm and 1.73µm, respectively.

The average crystalline grain size for the coated samples was calculated to be 128 nm and 121 nm in the coatings for an increase in hardness and adhesion, respectively. It was found that the crystalline grain size was smaller at 300W and 6.7sccm, and larger at 370W and 4.7sccm.

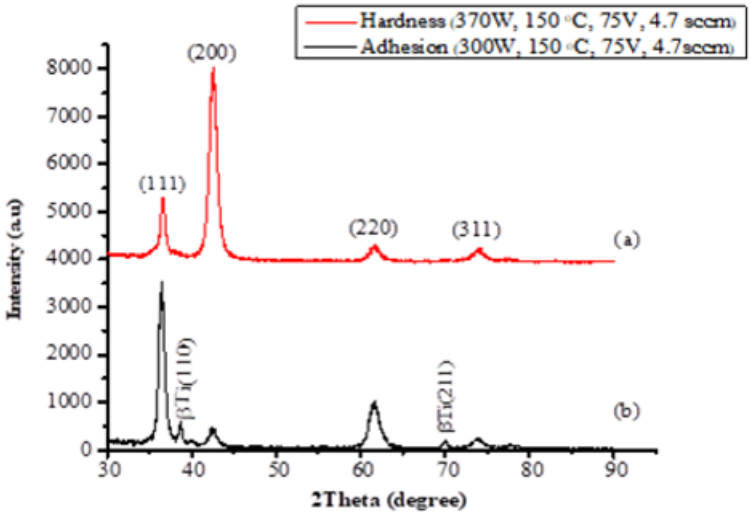

Figure 6. The XRD of TiN coatings: (a) 370W, 150 °C, 75V, 4.7sccm, (b) 300W, 150 °C, 75V, 6.7sccm

3.2.3 Microstructural Analysis Using FESEM, EDS and AFM

The FESEM micrographs and EDS of the cross-sections of the coated samples at different optimized parameters for hardness and adhesion strength are shown in Figures 7 and 8. The surface morphology of the coated Ti-27at. %Nb samples with the optimum parameters for hardness at 370W, 150°C, 100V, 4.7 sccm and adhesion at 300W, 150°C, 100V, 6.7 sccm are shown in Figure 7. It was found that the nanostructure morphology is influenced by DC power and nitrogen flow rate. Figure 7 (a) morphology revealed a lenticular-like structure with scanty pyramid-like grains at a nitrogen flow rate of 4.7sccm and DC power at 370W, while a more lenticular-like structure is revealed at 6.7sccm and 300W as shown in figure 7(b). Since the surface and cross-sectional morphologies of TiN films are significantly related to the preferred growth orientation (Zhang, *et al.*, 2019), it can be concluded that with a relatively low nitrogen flow rate of 4.7 sccm and relatively high DC power of 370W, the (200)-oriented TiN nanoparticles outgrew as shown in Figure 6(a). When nitrogen flow rate was increased to 6.7 sccm, more titanium atoms sputtered to react with all nitrogen atoms, and therefore the lenticular-like (111)-oriented TiN nanoparticles dominate (Zhang, *et al.*, 2019), as shown in Figure 6(b). Figures 8(a) and (b) show the coating thickness of the Ti interlayer and TiN coating from a cross-sectional FE-SEM micrograph and an EDS elemental line scan of a Ti/TiN film deposited at optimized parameters of 370W, 150°C, 100V, 4.7 and 300W, 150 °C, 100V, 6.7sccm on a Ti-27at percent Nb substrate for hardness and adhesion strength respectively. The interlayer and top layer thicknesses for hardness coating are 0.57µm and 1.73µm, while the thicknesses for adhesion coating are 0.5µm and 1.92µm.

The TiN films have a columnar structure with no cavities throughout their thickness, as seen in Figure 8. This development mechanism is comparable to the TiN film growth method described in the literature (Rahman et al., 2005). Understanding the oxidation process of these films depends on morphological research since oxygen can permeate via the spaces that exist between the columns and grain boundaries. The oxidation

Received: 03-02-2025 / Accepted: 10-03-2025 / Published: 24-05-2025

https://doi.org/10.70118/ujet.2025.0202.09

rate in the binary TiN system is significantly influenced by the coatings' shape. Mahalingam et al. (2013) state that films with a pronounced columnar shape oxidize more quickly than those with a finely-grained, dense architecture.

N, O, Ti, and Nb are the elements that are present in the cross-sectional line scan of EDX, which starts at the substrate surface and finishes in the top layer. The elemental distribution profile is displayed in Figure 8. All of the element line profiles' behaviours are shown in the Ti and TiN coating zones. The oxygen and nitrogen contents were found to be present and to have progressively grown from the substrate to the final TiN layer, according to the data. The Ti interlayer is fragile, and nitrogen doping is necessary to make it stronger and harder (Mubarak and Hamzah, 2006). The dissolution of nitrogen in the α-Ti lattice leads to the solid solution hardening in the interlayer, which is the source of the Ti interlayer's increasing hardness in the Ti/TiN coating as the quantity of nitrogen doping increases (Chunyan et al., 2009). The enhanced adhesion strength can be ascribed to the higher strength of Ti interlayer-influenced nitrogen. As the native oxide deposit on the substrate's surface is broken down by the Ti interlayers' oxygen acquisition, the adherence of the coating and substrate both improve. The adhesion strength of the TiN coating is improved with nitrogen gas because it strengthens the Ti interlayer and increases its capacity to sustain it.

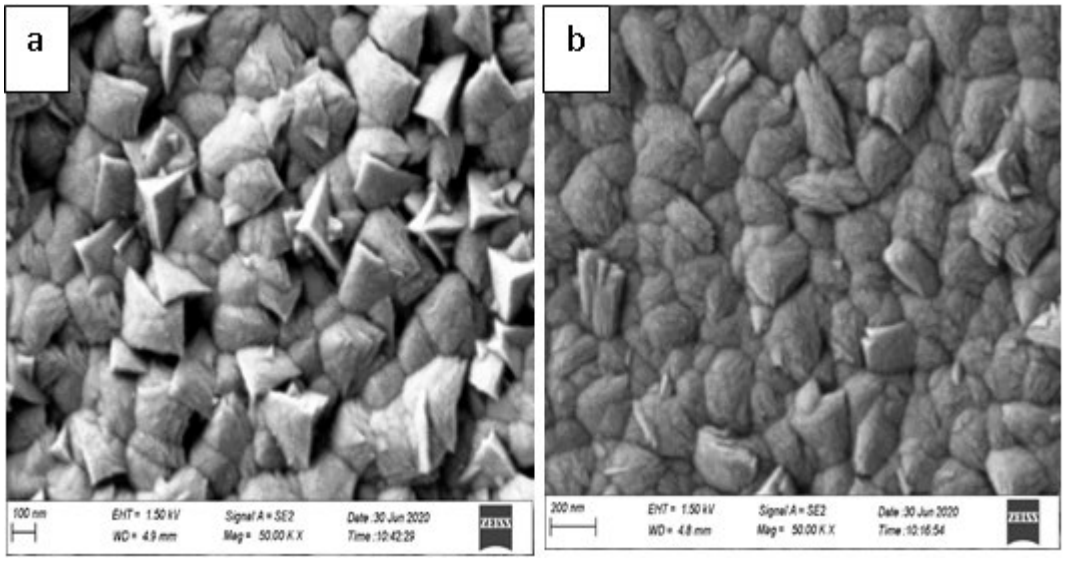

Figure 7. FESEM micrographs of TiN coating with optimum parameters for hardness at (a) 370W, 150°C, 100V, 4.7 sccm and adhesion at (b) 300W, 150°C, 100V, 6.7 sccm

Received: 03-02-2025 / Accepted: 10-03-2025 / Published: 24-05-2025
https://doi.org/10.70118/ujet.2025.0202.09

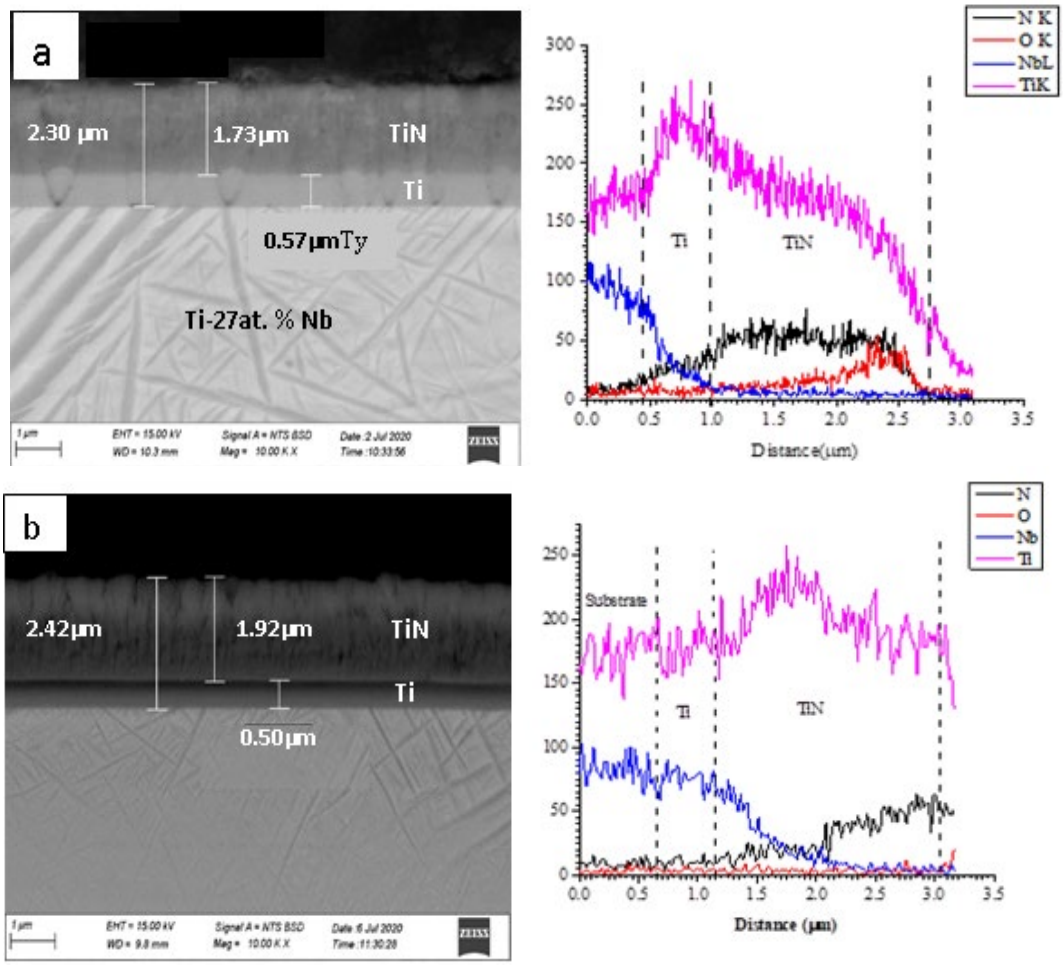

Figure 8. An EDS line scan and cross-sectional FESEM micrograph of TiN-coating were used to measure adhesion and hardness at (b) 300W, 150oC, 100V, 6.7 sccm, and (a) 370W, 150oC, 100V, 4.7 sccm.

3.3 Analysis of Ti-25at. %Ta Alloy Uncoated and Coated

3.3.1 Analysis of Ti-25at. %Ta Alloy Uncoated

Figure 9 is an illustration of EBSD results obtained from scanning the as-received Ti-25at. %Ta alloy. The scanned area inverse pole figure showed that the as-received specimen was dominated by β-phase with some traces of α-phase particles within the matrix as shown in Figure 9(a). The composition was found to be consistent with Ti–Ta alloy equilibrium binary phase diagrams. The phase fraction mapping revealed that the β phase is dominant with a higher number fraction of 0.987, as illustrated in Figure 9(b). According to the EBSD results, the average grain size is 72µm, and the grain size distribution is shown in Figure 10.

Received: 03-02-2025 / Accepted: 10-03-2025 / Published: 24-05-2025

https://doi.org/10.70118/ujet.2025.0202.09

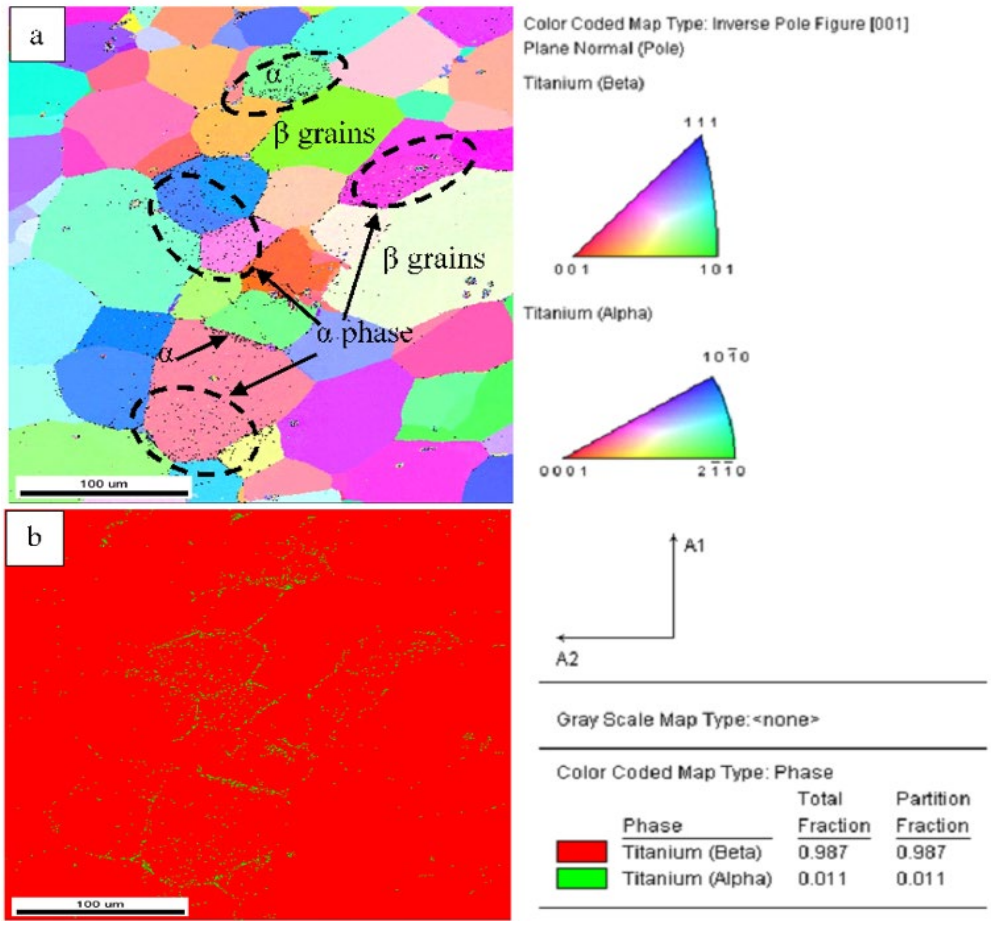

Figure 9. EBSD inverse pole figure orientation maps of the Ti-25at. %Ta sample showing random texture, a phase and equiaxed β grains inverse pole figure (IPF) map and (b) phase fraction mapping

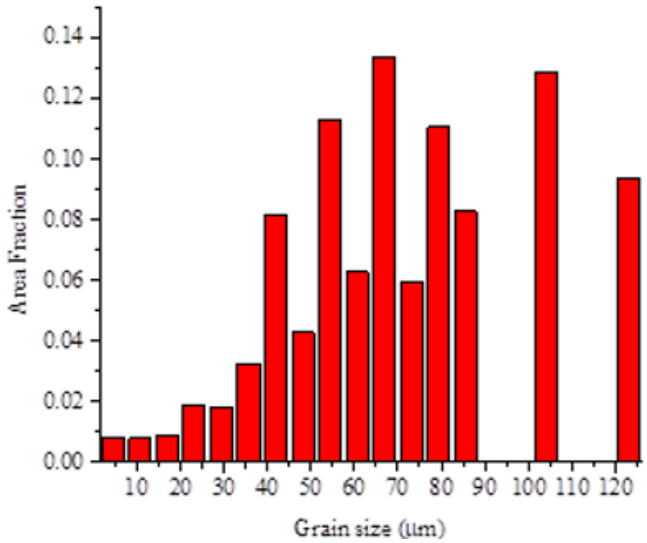

Figure 10. Grain size distribution of uncoated Ti-25at. %Ta

Figure 11 shows a FESEM micrograph of the as-received Ti-25at %Ta specimen, which shows α lath growing from grain boundaries into the β matrix; this could result from heat treatment quenching, which allowed α lamellae formed during the early cooling stage to be identified (Obasi *et al.*, 2012). The α phase formation is influenced by the percentage of elemental composition in the Ti-Ta alloy. It is only at a Ta content of less than 30% and a sintering temperature of less than 1500°C can the α phase be seen (Liu *et al.*, 2015). The α phase was therefore formed due to the Ta content of the alloy, which is 25at%.

Six different points were identified for EDS scanning. The results revealed that the white areas with dark spots, such as spot 5 are a pore with high percentages of oxygen, denoting oxides. Dark area 2 and spot 3 are identified as α-Ti-rich regions with a high percentage of Ti. Spots 1, 4, and 6 are the matrices with homogeneous elemental distribution. Figure 12 displays the elemental distribution EDS graphs for the Ti-

Received: 03-02-2025 / Accepted: 10-03-2025 / Published: 24-05-2025

https://doi.org/10.70118/ujet.2025.0202.09

25%Ta sample.

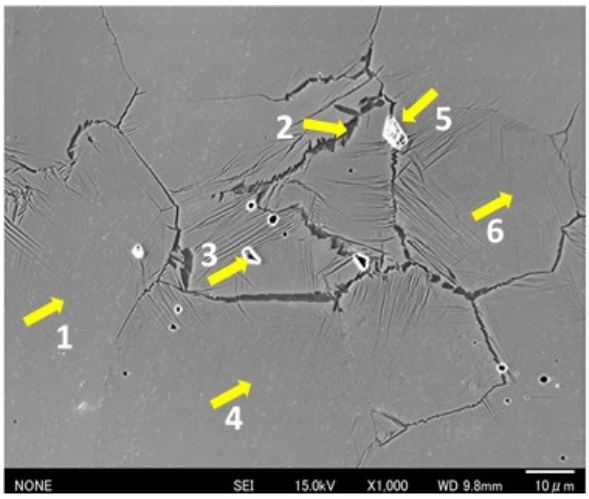

Figure 11. FESEM of elemental distribution of uncoated Ti-25at. %Ta alloy

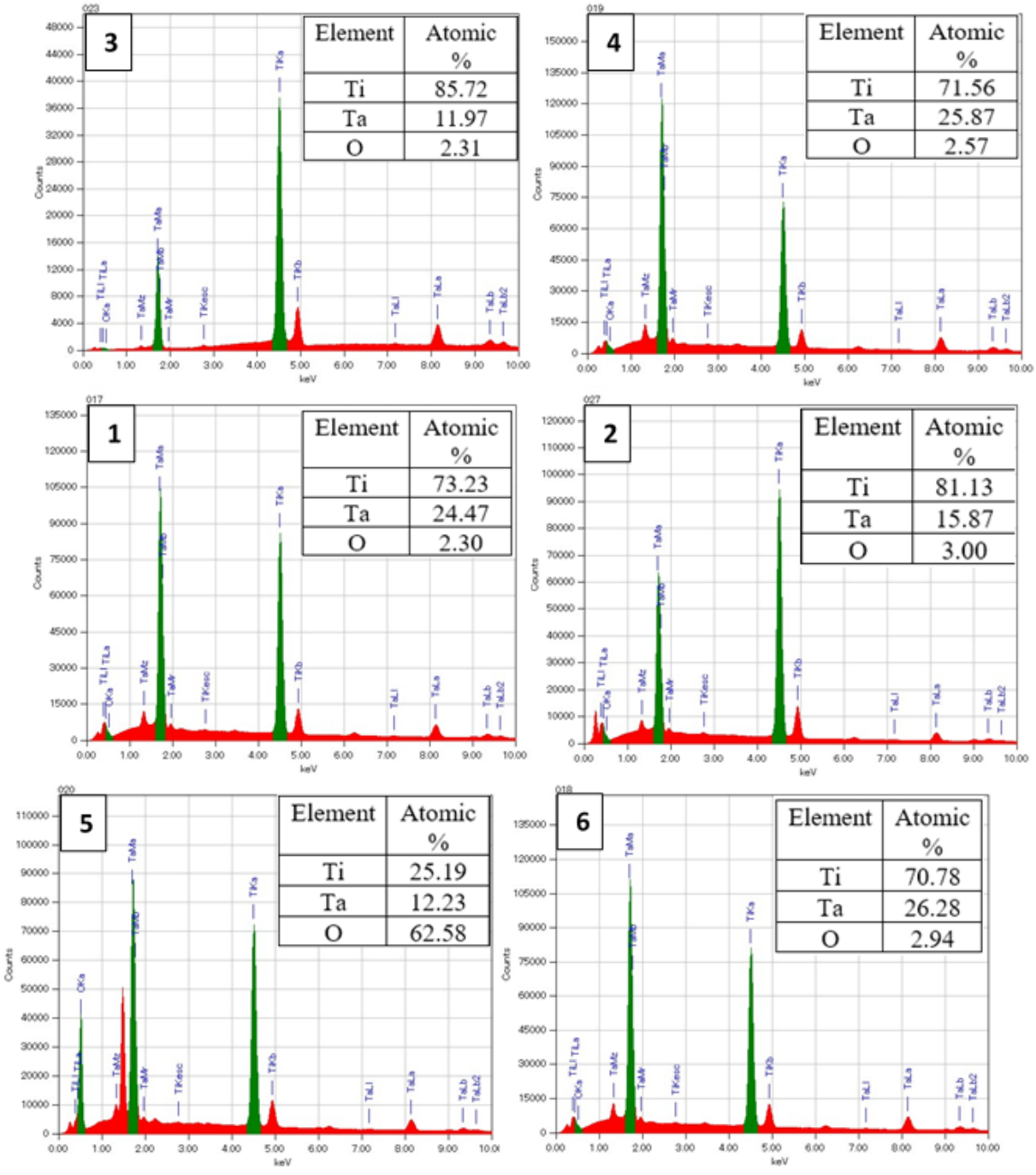

Received: 03-02-2025 / Accepted: 10-03-2025 / Published: 24-05-2025
https://doi.org/10.70118/ujet.2025.0202.09

Figure 12. EDS of the elemental distribution of Ti-25%Ta sample

Figure 13 shows the X-ray diffraction patterns of the Ti-25%Ta alloy. The XRD results revealed that the alloy comprised of α-phase and β-phase. The β -phase is dominant due to the Ta elements stabilizing effect on the β -phase. In the binary Ti–Ta β matrix, the Ta content influences the α -phase formation due to the sensitivity of α -phase to Ta in the binary Ti–Ta β matrix (Bahador *et al.*, 2019).

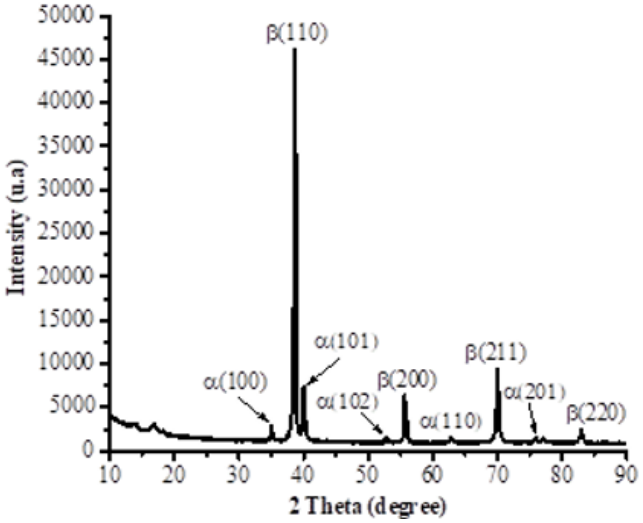

Figure 13. XRD spectrum of Ti-25at. %Ta sample

3.3.2 XRD ***Analyses of Ti-25at. %Ta Sample Coated with Ti/TiN***

To obtain better hardness and adhesion strength, Ti/TiN films were deposited on a Ti-25at%Ta substrate at various ideal settings. These parameters, which included 370W, 150OC, 75V, 4.7sccm, and 300W, 150OC, 75V, 6.7sccm, are shown in Figure 23(a) and (b), respectively. The coating exhibits peaks (111), (200), (220), and (311), which are located at 2θ = 36.61^{O}, 42.53^{O}, 61.90^{O,} and 74.00^{O}. Figure 14 (a) shows an osbornite phase, and the peak intensities indicate that the preferred orientations are the same as those of the TiN phase, while Figure 14(b) exhibits a typical TiN phase of face-centered cubic (FCC) crystal planes. When comparing the (111) plane to the other orientations in Figure 14, the sharp peak is recognized as (a). This is because the strain energy (111) plane is favored by the energy injected into the growing film by the ion bombardment at a DC power of 300W and a bias voltage of 50V. However, strain energy becomes the main energy in the film's development as due to the increased 370W and 75V, which enhance the deposited ion energy. Instead, as Figure 14(b) illustrates, stopping energy (220) takes center stage. This suggests that the ion energy is high enough to allow for the observation of the (220) preferred orientation (Arshi et al., 2012).

It was discovered from the research done by Escalona et al. (2021) that surface energy and strain energy had an impact on the film thickness. At thinner TiN thicknesses, the TiN (200) orientation with the lowest surface energy is selected, as the surface energy term is substantial. The strain energy difference between various lattice planes becomes dominant as the film thickness increases, indicating the preferred orientation (111); this is consistent with the thickness measurements of 1.91µm for surface hardness and 1.78µm for adhesion strength samples in the TiN coatings.

The average crystalline grain size for the coated samples was calculated to be 189 nm and 74 nm in the coatings for an increase in adhesion and hardness, respectively.

Received: 03-02-2025 / Accepted: 10-03-2025 / Published: 24-05-2025

https://doi.org/10.70118/ujet.2025.0202.09

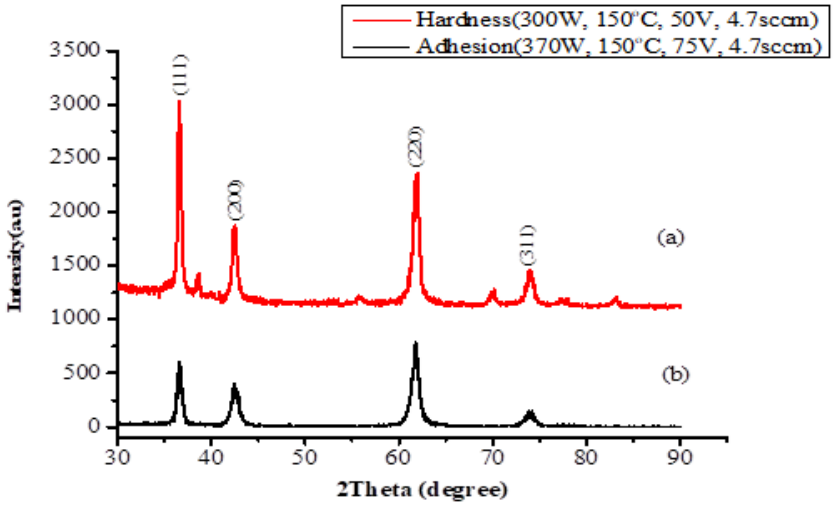

Figure 14. The XRD patterns of TiN coatings: (a) 300W, 150°C, 50V, 4.7sccm, (b) 370W, 150°C, 75V, 4.7sccm

3.3.3 Microstructural Analysis FESEM, EDX and AFM of Ti-25at. %Ta Sample Coated with Ti/TiN

Figures 15 and 16 display the FESEM micrographs and EDX cross-sections of the TiN coating at various optimal values for adhesion strength and surface hardness. Figure 15 displays the surface morphology of the Ti/TiN coated on Ti-25 at %Ta samples with ideal parameters for adhesion at 370W, 150 °C, 75V, 4.7sccm, and hardness at 300W, 150 °C, 50V, 4.7sccm. This shows how the best deposition parameters affect the nanostructure morphology. The combinations of optimal parameters for coatings are distinguished by DC power and substrate bias voltage, which may likely influence the nanostructure of the coatings.

Figure 15(a) morphology revealed a pyramid-like grains structure at a DC power of 300W and a bias voltage of 50V, while a more lenticular-like structure with scanty pyramid-like grains is revealed at 370W and 70V as shown in Figure 15(b). Based on the strong correlation between the preferred growth orientation and the surface and cross-sectional morphologies of TiN films (Zhang et al., 2019), it can be inferred that at 300 W of DC power and 50 V of substrate bias, (111)-oriented TiN nanoparticles with pyramid-like grain structures outgrow, as depicted in Figure 15(a). However, with higher DC power of 370W and a substrate bias voltage of 75V, the (220)-oriented TiN nanoparticles of faceted structure dominate as shown in Figure 15(b).

Figures 16(a) and (b) show the coating thickness of Ti interlayer and TiN coating from a cross-sectional FESEM micrograph and an EDS line scan of a Ti/TiN film deposited at optimised parameters of 300W, 150 °C, 50V, 4.7 and 370W, 150 °C, 75V, 4.7 sccm on a Ti-25at% Ta substrate for hardness and adhesion respectively. The interlayer and top layer thicknesses for the hardness coating are 0.59µm and 1.91µm, while the thicknesses for adhesion coating are 0.53µm and 1.78µm.

As seen in Figure 16, the TiN films have a columnar structure with no cavities throughout their thickness. The process of development is akin to that of TiN films documented in scholarly works (Rahman et al., 2005). Since oxygen can penetrate via the spaces between the columns and grain boundaries, a morphological investigation is essential to understanding how these films oxidize. The oxidation rate in the binary TiN system is highly dependent on the coating shape. Compared to films with a dense and finely grained morphology, those with a pronounced columnar shape oxidize more quickly. (Mahalingam, *et al.*, 2013).

N, O, Ti, and Ta are the elements found in the EDX cross-sectional line scan from the substrate surface to the top layer. In Figure 16, the diffusion rate of each constituent is shown. In the Ti and TiN coating zones, all the element line profiles are visible. The element concentration did, however, progressively rise from the substrate to the final TiN layer, according to the research. Nitrogen doping is necessary to strengthen and harden the Ti interlayer since it is brittle (Mubarak and Hamzah, 2006). As the amount of nitrogen doping grows, the hardness of the Ti interlayer in the Ti/TiN coating also increases. This is undoubtedly caused by nitrogen dissolving in the α-Ti lattice, which results in the solid solution in the interlayer (Chunyan *et al.*, 2009).

The stronger Ti interlayer-influenced nitrogen was responsible for the improved adhesion strength. As the native oxide film on the substrate surface is broken down by the Ti interlayers that have taken up oxygen, the adhesion of the substrate and coating both get better. Nitrogen gas increases the strength of the Ti interlayer and makes it able to support TiN coating more, which improves adhesion strength.

Received: 03-02-2025 / Accepted: 10-03-2025 / Published: 24-05-2025

https://doi.org/10.70118/ujet.2025.0202.09

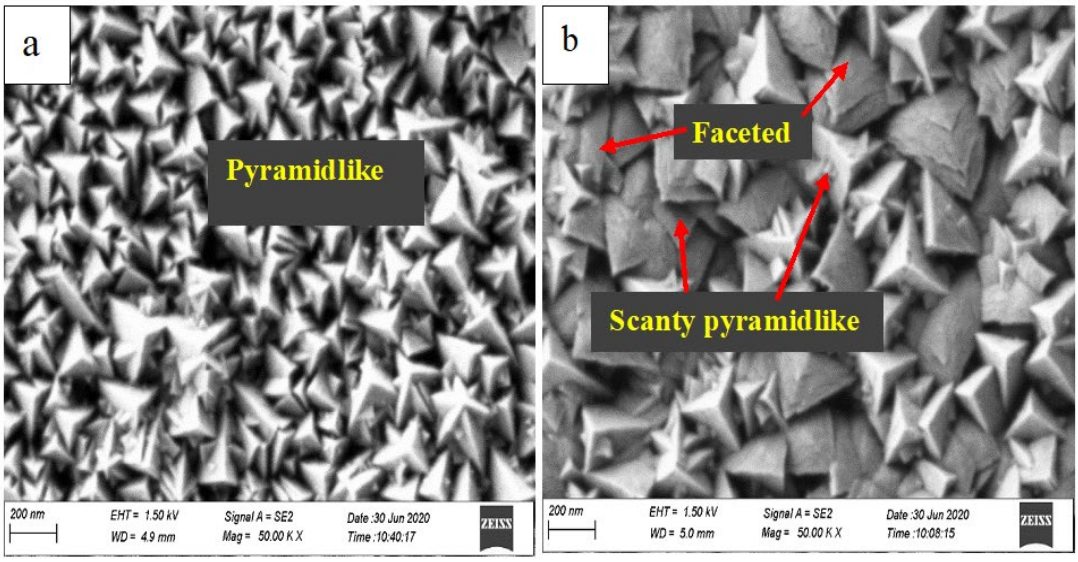

Figure 15. FESEM micrographs of Ti/TiN coating with optimum parameters for hardness at (a) 300W, 150^{O}C, 50V, 4.7sccm and adhesion at (b) 370W, 150^{O}C, 75V, 4.7sccm

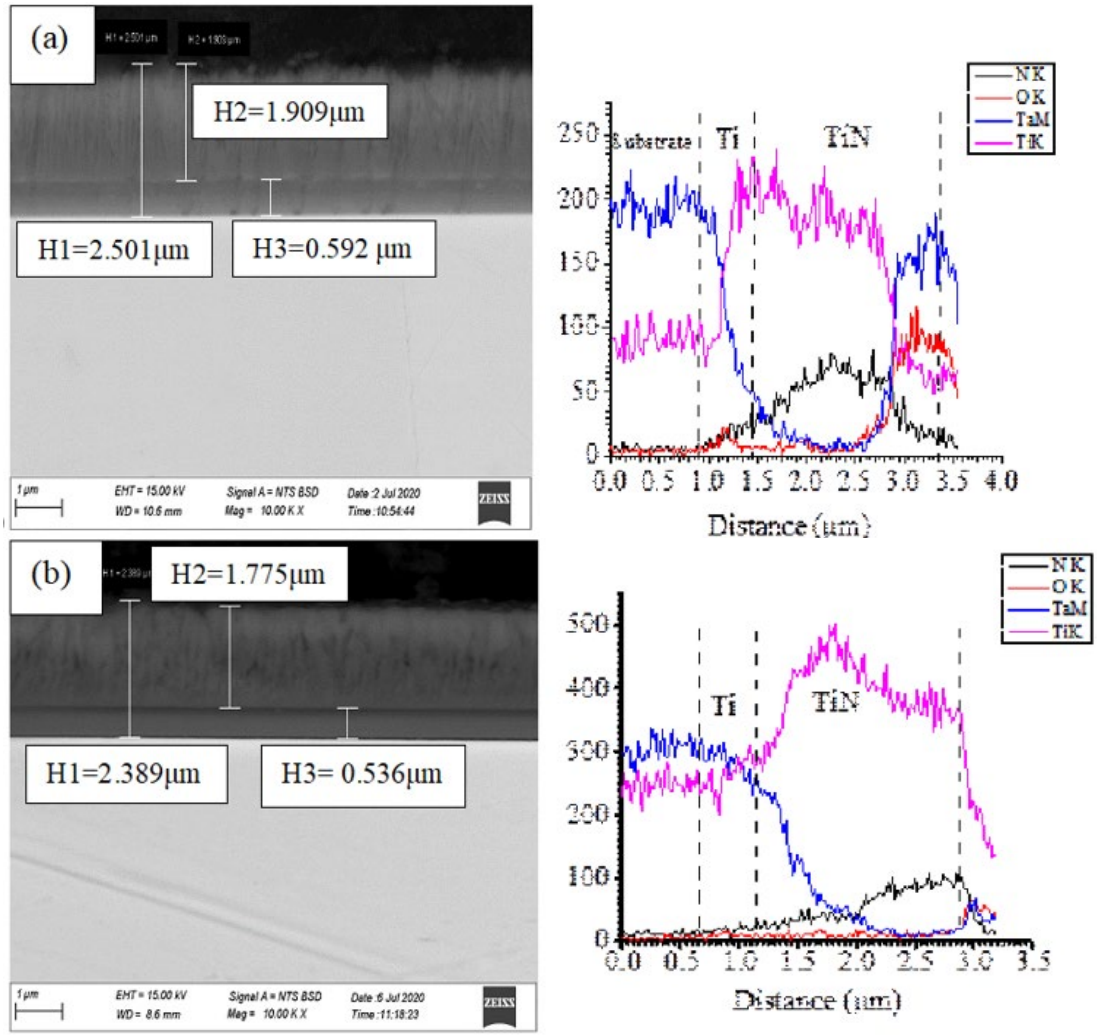

Figure 16. Cross-sectional FESEM micrograph and EDS elemental line scan of the coating for hardness at (a) 300W, 150^{O}C, 50V, 4.7sccm and adhesion at (b) 370W, 150^{O}C, 75V, 4.7sccm

The microstructure and micro texture of the uncoated Ti-27 at% Nb as determined by EBSD showed equiaxed β grains and random texture. Inside the equiaxial β grains, the α phase is formed as fine and dominant coarse acicular facets. The phase fraction mapping revealed that β phase is dominant with a higher number fraction of 0.811. The EBSD generated results shows that the average grain size is 38µm.

Received: 03-02-2025 / Accepted: 10-03-2025 / Published: 24-05-2025
https://doi.org/10.70118/ujet.2025.0202.09

The coated Ti-27at. %Nb alloy shown in Figure 7, displays the surface shape of the Ti/TiN coated on Ti-27at. %Nb samples with optimized values for adhesion at 300W, 150^{o}C, 100V, 6.7 sccm, and hardness at 370W, 150^{o}C, 100V, 4.7 sccm. It was found that the nanostructure morphology is influenced by nitrogen flow rate and DC power. The morphology revealed a lenticular-like structure with scanty pyramid-like grains at nitrogen flow rate of 4.7sccm and DC power at 370W. The interlayer and top layer thicknesses for hardness coating are 0.57µm and 1.73µm, while the thicknesses for adhesion coating are 0.50µm and 1.92µm.

The EBSD analysis of the uncoated Ti-25at%Ta alloy revealed that the specimen was mostly composed of β-phase particles, with some α-phase particles present in the matrix. The EBSD measurements show that the average grain size is 72µm. The X-ray diffraction pattern of Ti/TiN films deposited on Ti-25at%Ta substrate at various optimal parameters of 370W, 150^{O}C, 75V, 4.7sccm and 300W, 150^{O}C, 75V, 6.7sccm achieved higher hardness and adhesion strength. The average crystalline grain size for the coated samples was calculated to be 189 nm and 74 nm in the coatings for increase in hardness and adhesion, respectively.

The coating thickness of Ti interlayer and TiN coating from a cross-sectional FESEM micrograph and an EDS line scan of a Ti/TiN film deposited at optimised parameters of 300W, 150^{o}C, 50V, 4.7 and 370W, 150^{o}C, 75V, 4.7 sccm on a Ti-25at% Ta substrate for adhesion strength and surface hardness respectively. The interlayer and top layer thicknesses for the hardness coating are 0.59µm and 1.91µm, while the thicknesses for adhesion coating are 0.53µm and 1.78µm.

The improved adhesion strength was caused by the stronger Ti interlayer-influenced nitrogen. As the native oxide film on the substrate surface is broken down by the Ti interlayers that have taken up oxygen, the adhesion of the substrate and coating both get better. Nitrogen gas increases the strength of the Ti interlayer and makes it able to support the TiN coating more, which improves adhesion strength.

In another investigation conducted by (Arudi & Balogun, 2024) to compare the results of this study to the previous results conducted on a similar alloy (Ti-51at. %Ni), it was discovered that the XRD analysis of the uncoated Ti-51at. %Ni alloy suggested that there are B2 austenite, R- martensite and $TiNi_3$ intermetallic present in the alloy. The equiaxed grains and random texture are irregularly shaped with an average size of 134µm as revealed by the EBSD results. The XRD patterns of the TiN coating with optimum parameters of 370W, 50V, 4.7sccm, 100^{o}C for hardness and 370W, 150^{o}C, 75V, 4.7 sccm for adhesion strengths. Results of the analyses from the surface structure evaluation revealed a homogeneous coating which shows the detection of an osbornite. The thickness of the interlayer and top layer for hardness coating are 0.458µm and 1.585µm, while the thickness of the interlayer and top layer for adhesion coating are 0.571µm and 1.706µm, respectively.

4.0 Conclusions

The effect of the recommended parameter combinations on crystallite structure was established and the average crystallites (grain) size of the improved samples as presented by the XRD analysis were determined. The various thicknesses of coated Ti-27at. %Nb and Ti-25at. %Ta samples that give optimal adhesion strength are 1.92µm, 1.78 µm and for optimal surface hardness are 1.73µm, 1.91 µm respectively. Results of AFM analysis showed that Ti/TiN coated Ti-27at. %Nb to obtain optimal adhesion has lower surface roughness (Ra) of 27.04nm, than the coating to obtain optimal hardness which is 44.07nm while Ti/TiN coated Ti-25at. %Ta to obtain optimal hardness has lower surface roughness of 32.20nm than the coating for optimal adhesion with roughness of 33.56nm.

5.0 Recommendations

Detail study of the growth mechanism of the Ti/TiN layers on each of the two alloys will be useful in order to relate it to its final properties.

Coated Ti-51at. %Ni alloy could be used as an alternative to both samples because of its surface hardness and adhesion strength resulting from the similarity in coating parameter combinations.

References

Arshi, N., Lu, J., Joo, Y. K., Lee, C. G., Yoon, J. H. and Ahmed, F. (2012). Study on structural, morphological and electrical properties of sputtered titanium nitride films under different argon gas flow. Materials Chemistry and Physics. 134(2-3), 839-844.

Arudi, I. S., Balogun, S., (2024). Enhanced microstructure of Coated Ti-51at. %Ni coated TiN using DC PVD magnetron sputtering technique. Nile Journal of Engineering & Applied Sciences. 2(2), 250-261

Bahador, A., Kariya, S., Umeda, J., Hamzah, E. and Kondoh, K. (2019). Tailoring microstructure and properties of a superelastic Ti–Ta alloy by incorporating spark plasma sintering with thermomechanical processing. Journal of Materials Engineering and Performance. 28(5), 3012-3020.

Brunette, D. M., Tengvall, P., Textor, M. and Thomsen, P. (2012). Titanium in medicine: material science, surface science, engineering, biological responses and medical applications. Springer Science & Business Media.

Received: 03-02-2025 / Accepted: 10-03-2025 / Published: 24-05-2025

https://doi.org/10.70118/ujet.2025.0202.09

Chien, C., Liu, C., Kuo, T., Wu, C. and Hong, T. (2016). Bioactivity of fluorapatite/alumina composite coatings deposited on Ti6Al4V substrates by laser cladding. Applied Physics A. 122(4), 303.

Chunyan, Y., Linhai, T., Yinghui, W., Shebin, W., Tianbao, L. and Bingshe, X. (2009). The effect of substrate bias voltages on impact resistance of CrAlN coatings deposited by modified ion beam enhanced magnetron sputtering. Applied Surface Science. 255(7), 4033-4038.

de Souza, K. A. and Robin, A. (2003). Preparation and characterization of Ti–Ta alloys for application in corrosive media. Materials Letters. 57(20), 3010-3016.

Electrochemistry, P., Elements, C., Equivalent, C. and Models, C. (2010). Basics of electrochemical impedance spectroscopy. Appl Note AC. 286, R491-497.

Escalona, M., Bhuyan, H., Ibacache, S., Retamal, M., Saikia, P., Borgohain, C., Valenzuela, J., Veloso, F., Favre, M. and Wyndham, E. (2021). Study of titanium nitride film growth by plasma enhanced pulsed laser deposition at different experimental conditions. Surface and Coatings Technology. 405, 126492.

Hermawan, H., Ramdan, D. and Djuansjah, J. R. (2011). Metals for biomedical applications Biomedical engineering-from theory to applications InTech.

Liu, Y., Li, K., Wu, H., Song, M., Wang, W., Li, N. and Tang, H. (2015). Synthesis of Ti–Ta alloys with dual structure by incomplete diffusion between elemental powders. journal of the mechanical behavior of biomedical materials. 51, 302-312.

Lopes, E. S., Cremasco, A., Contieri, R. and Caram, R. (2011). Effects of aging heat treatment on the microstructure of Ti-Nb and Ti-Nb-Sn alloys employed as biomaterials. Proceedings of the 2011 Advanced Materials Research: Trans Tech Publ, 61-64.

Mahalingam, T., Dhanasekaran, V., Devadason, S. and Chu, J. (2013). Preparation and Characterization of Electrosynthesized ZnSeTe Thin Films. ECS Transactions. 45(9), 19.

Manivasagam, G., Dhinasekaran, D. and Rajamanickam, A. (2010). Biomedical Implants: Corrosion and its Prevention-A Review. Recent Patents on Corrosion Science.

Massalski, T. B., Okamoto, H., Subramanian, P. and Kacprzak, L. (1990). Binary alloy phase diagrams. vol. 3. ASM International, 1990. 1485.

Mubarak, A. and Hamzah, E. (2006). Influence of Nitrogen Gas Flow Rate on The Microstructural and Mechanical Properties of Tin Deposited Carbon Steel Synthesized by Cae. ASEAN Journal on Science and Technology for Development. 23(4), 239-251.

Obasi, G., Birosca, S., Fonseca, J. and Preuss, M. (2012). Effect of b grain growth on variant selection and texture memory effect during a! b! a phase transformation in Ti–6 Al–4 V. Acta Mater. 60, 1048-1058.

Rahman, M., Haider, J., Dowling, D., Duggan, P. and Hashmi, M. (2005). Deposition of magnetron sputtered TiN+ MoSx coating with Ti–TiN graded interlayer. Surface and Coatings Technology. 200(1-4), 1071-1075.

Štěpán, P. and Losertová, M. (2011). Microstructure Properties of TiNb Alloys Prepared by Plasma metallurgy, Website: www.mtf.stuba.sk/buxus/docs/internetovy_casopis/2011/mimoriadne_cislo/stepan_losertova.pdf, Date Visited: 24/05/2025.

Tugulu, S., Löwe, K., Scharnweber, D. and Schlottig, F. (2010). Preparation of superhydrophilic microrough titanium implant surfaces by alkali treatment. Journal of materials science: Materials in medicine. 21(10), 2751-2763.

Wang, G. and Zreiqat, H. (2010). Functional coatings or films for hard-tissue applications. Materials. 3(7), 3994-4050.

Wang, L., Lin, Z., Wang, X., Shi, Q., Yin, W., Zhang, D., Liu, Z. and Lu, W. (2014a). Effect of aging treatment on microstructure and mechanical properties of Ti27Nb2Ta3Zr β titanium alloy for implant applications. Materials Transactions. 55(1), 141-146.

Xu, G., Hibino, Y., Nishimura, Y. and Yatsuzuka, M. (2013). Hydrogenated amorphous carbon formation with plasma-immersion ion plating. Surface and Coatings Technology. 169, 299-302.

Zhang, S., Yan, F., Yang, Y., Yan, M., Zhang, Y., Guo, J. and Li, H. (2019). Effects of sputtering gas on microstructure and tribological properties of titanium nitride films. Applied Surface Science. 488, 61-69.

Received: 03-02-2025 / Accepted: 10-03-2025 / Published: 24-05-2025

https://doi.org/10.70118/ujet.2025.0202.09